An Exploratory Flow Reactor Study of H2S Oxidation at 30-100 Bar

Song, Yu; Hashemi, Hamid; Christensen, Jakob Munkholt; Zou, Chun; Haynes, Brian S.; Marshall, Paul; Glarborg, Peter

Published in:
International Journal of Chemical Kinetics

Link to article, DOI:
10.1002/kin.21055

Publication date:
2017

Document Version
Peer reviewed version

An Exploratory Flow Reactor Study of H_2S Oxidation at 30–100 Bar

YU SONG,[1,2] HAMID HASHEMI,[1] JAKOB MUNKHOLT CHRISTENSEN,[1] CHUN ZOU,[2] BRIAN S. HAYNES,[3] PAUL MARSHALL,[4] PETER GLARBORG[1]

[1]*Department of Chemical and Biochemical Engineering, Technical University of Denmark, DK-2800 Kgs. Lyngby, Denmark*

[2]*State Key Laboratory of Coal Combustion, Huazhong University of Science and Technology, Wuhan, 430074, People's Republic of China*

[3]*School of Chemical and Biomolecular Engineering, University of Sydney, Sydney, Australia*

[4]*Department of Chemistry and Center for Advanced Scientific Computing and Modeling (CASCaM), University of North Texas, Denton, TX, 76203-5017*

Received 4 July 2016; revised 30 September 2016; accepted 1 October 2016

DOI 10.1002/kin.21055
Published online 9 November 2016 in Wiley Online Library (wileyonlinelibrary.com).

ABSTRACT: Hydrogen sulfide oxidation experiments were conducted in O_2/N_2 at high pressure (30 and 100 bar) under oxidizing and stoichiometric conditions. Temperatures ranged from 450 to 925 K, with residence times of 3–20 s. Under stoichiometric conditions, the oxidation of H_2S was initiated at 600 K and almost completed at 900 K. Under oxidizing conditions, the onset temperature for reaction was 500–550 K, depending on pressure and residence time, with full oxidization to SO_2 at 550–600 K. Similar results were obtained in quartz and alumina tubes, indicating little influence of surface chemistry. The data were interpreted in terms of a detailed chemical kinetic model. The rate constants for selected reactions, including SH + $O_2 \rightleftarrows SO_2$ + H, were determined from ab initio calculations. Modeling predictions generally overpredicted the temperature for onset of reaction. Calculations were sensitive to reactions of the comparatively unreactive SH radical. Under stoichiometric conditions, the oxidation rate was mostly controlled by the SH + SH branching ratio to form H_2S + S (promoting reaction) and HSSH (terminating). Further work is desirable on the SH + SH recombination and on subsequent reactions in the S_2 subset of the mechanism. Under oxidizing conditions, a high O_2 concentration (augmented by the high pressure) causes the termolecular reaction SH + O_2 + $O_2 \rightarrow$ HSO + O_3 to become the major consumption step for SH, according to the model. Consequently, calculations become very sensitive to the rate constant and product channels for the $H_2S + O_3$ reaction, which are currently not well established. © 2016 Wiley Periodicals, Inc. Int J Chem Kinet 49: 37–52, 2017

Correspondence to: Peter Glarborg; e-mail: pgl@kt.dtu.dk.

Supporting Information is available in the online issue at www.wileyonlinelibrary.com.

INTRODUCTION

Hydrogen sulfide (H_2S) is a by-product from cleaning of natural gas and synthesis gas produced from

gasification of coal or biomass, from hydrodesulfurization of light hydrocarbons, and from upgrading heavy oils and coals. It is also released from sulfur-containing fuels during pyrolysis or formed under very reducing conditions in combustion processes. The medium to high-temperature chemistry of H_2S has received attention due to its importance in combustion, in the Claus process, and as a potential hydrogen source [1,2]. The H/S system has been investigated for both H_2S pyrolysis and H_2 sulfidation [3–10]. Despite some remaining uncertainties, available experimental results are described satisfactorily by a detailed reaction mechanism [8].

A wide range of studies have dealt with H_2S conversion in the presence of oxygen. Wilson and Hirst [11] discuss atmospheric oxidation of H_2S, whereas early investigations of oxidation at elevated temperatures were reviewed by Cullis and Mulcahy [12]. Experimental results have been reported for explosion limits and induction times in static reactors [13–17], oxidation in flow reactors [18], induction times in shock tubes for H_2S [19] and H_2/H_2S mixtures [20], flame speeds [21–24], and structures of premixed [25–32] and diffusion flames [33].

Early modeling efforts for H_2S oxidation [19,34] largely had to rely on estimated rate constants for the sulfur subset. More recently, Haynes and coworkers investigated the chemistry of H_2S pyrolysis and oxidation in a series of modeling studies [8,18], supported by ab initio calculations for key reactions [35–39]. The mechanism of Zhou et al. [18] was adopted and slightly revised by Mathieu et al. [20] who studied the impact of H_2S on ignition of H_2 over large pressure (1.6–33 atm) and temperature (1045–1860 K) ranges. Bongartz and Ghoniem [40] used the mechanism of Zhou et al. as a starting mechanism for a more thorough optimization study, using rate constants for 15 reactions in the scheme as parameters when modeling a range of experimental data reported in the literature.

With the exception of the shock tube experiments from Frenklach et al. [19] and Mathieu et al. [20], results for H_2S oxidation at elevated pressures are scarce. The objective of the present study is to obtain experimental results for the oxidation of H_2S at high pressure (30–100 bar) as a function of temperature (600–925 K) and stoichiometry (lean to stoichiometric) and analyze them in terms of a detailed chemical kinetic model, based on the work of Zhou et al. [18].

EXPERIMENTAL

The experimental setup was a laboratory-scale high-pressure laminar flow reactor designed to approximate plug flow. The setup is described in detail elsewhere [41], and only a brief description is provided here. The system was used here for investigation of hydrogen sulfide oxidation at 30 bar and 100 bar pressure, respectively, and temperatures from 450 to 900 K.

The reactions took place in a tubular quartz reactor (inner diameter of 7.5 mm), enclosed in a stainless steel tube that acted as a pressure shell. Using a quartz tube and conducting the experiments at high pressure ensured a minimal contribution from heterogeneous reactions at the reactor wall. However, additional experiments were conducted in an alumina tube (Degussit AL23; inner diameter 6 mm) to assess the importance of surface reactions. The steel tube was placed in a tube oven with three individually controlled electrical heating elements that produced an isothermal reaction zone (±6 K) of 37–47 cm. The temperature profile in the flow reactor was measured by a thermocouple positioned in the void between the quartz/alumina reactor and the steel shell. Results for 30 bar are shown in Fig. 1, whereas the 100-bar profiles are available as the Supporting Information. The system was pressurized from the feed gas cylinders. The reactor pressure was monitored upstream of the reactor by a differential pressure transducer and controlled by a pneumatically actuated pressure-control valve positioned after the reactor. All gases used in the present experiments were high-purity gases or mixtures with certified concentrations. The total flow rate was 2.8 L min^{-1} (STP).

The product analysis was conducted by an online 6890N Agilent Gas Chromatograph (GC-TCD/FID from Agilent Technologies) with an overall relative measurement uncertainty in the range ±2–6%.

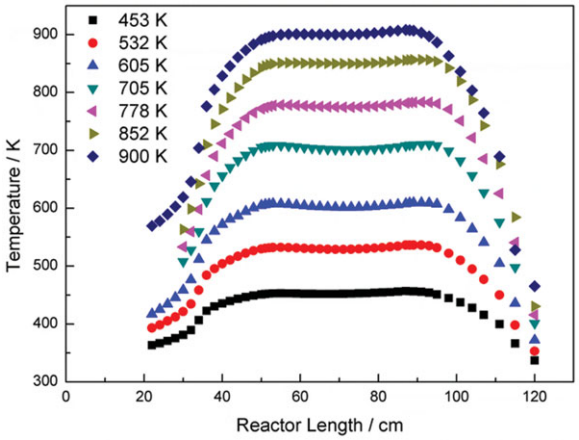

Figure 1 Measured temperature profiles along the reactor axis for 30 bar conditions.

Table I Thermodynamic Properties for Selected Species in the Sulfur Subset. Units are kcal mol^{-1} for H, and cal mol^{-1} K^{-1} for S and C_p. The temperatures for C_p are in K

Species	ΔH_{f298}	S_{298}	C_{p300}	C_{p400}	C_{p500}	C_{p600}	C_{p800}	C_{p1000}	C_{p1500}	
H_2S	−4.92	49.18	8.19	8.52	8.91	9.34	10.20	11.00	12.35	[48]
SH	34.23	46.73	7.74	7.59	7.49	7.46	7.59	7.85	8.34	[18,49]
S	66.19	40.11	5.66	5.57	5.44	5.32	5.21	5.13	5.06	[48]
SO	1.14	53.04	7.22	7.53	7.84	8.10	8.42	8.63	8.97	[48]
SO_2	−70.93	59.32	9.54	10.37	11.10	11.70	12.50	12.98	13.54	[48]
SO_3	−94.61	61.30	12.13	13.77	15.07	16.07	17.39	18.16	19.00	[48]
HSO	−5.20	57.75	8.54	9.21	9.91	10.53	11.43	12.08	12.90	[48]
HOS	−1.60	57.31	8.78	9.44	10.03	10.50	11.11	11.58	12.38	[48]
HSOH	−28.52	58.66	10.82	12.25	13.46	14.44	15.84	16.61	17.60	[43]
HOSO	−57.70	67.47	11.87	13.43	14.56	15.37	16.40	17.06	18.09	[50]
HSO_2	−33.80	63.00	11.94	13.68	14.99	15.98	17.28	18.05	18.98	[50]
HSOO	32.29	67.63	12.38	13.58	14.48	15.16	16.10	16.78	17.74	[38]
S_2	30.73	54.52	7.78	8.14	8.39	8.57	8.77	8.94	9.33	[48]
HSS	25.84	60.94	9.62	10.30	10.80	11.19	11.80	12.26	12.98	[8,36]
HSSH	3.70	61.61	11.63	12.90	13.83	14.57	15.72	16.62	18.02	[8,36]

The plug flow assumption was shown by Rasmussen et al. [41] to be a good approximation for the present operating conditions. The uncertainty in the gas temperature due to the effect of heat release from combustion was limited by a high level of dilution.

DETAILED KINETIC MODEL

The detailed chemical kinetic model for H_2S oxidation was adopted mostly from the recent study on H_2S oxidation by Zhou et al. [18]. The reaction mechanism consists of a H_2 subset [42] and a full description of the H/S/O reaction system [8,18,43–47].

Table I shows thermodynamic properties of selected species. Most of the data are drawn from the database of Goos et al. [48]. The heats of formation of key species such as SH, HSO, and HOS are in agreement within the uncertainty with recent high-accuracy theoretical results [51–53].

Selected reactions from the sulfur subset are listed in Table II. Below selected reactions are discussed in some detail, with emphasis on steps that may have a particular significance under the high-pressure conditions of the present study.

Most of the reactions of H_2S with the radical pool have been characterized experimentally and theoretically over a wider temperature range. For $H_2S + H$ (R2), $H_2S + O$ (R3, R4), and $H_2S + S$ (R12), we rely on rate constants determined by Marshall and coworkers [54,55,58]. The rate constant for $H_2S + OH$ (R5) was taken from the theoretical study by Ellingson and Truhlar [56]; it provides an explanation for the unusual temperature dependence of the reaction, and the calculated value is in good agreement with experiment [64–68]. The $H_2S + O$ reaction has two product channels, SH + OH (R3) and HSO + H (R4). The branching fraction $k_4/(k_3 + k_4)$ calculated by Goumri et al. [55] agrees with the reported low-temperature upper limit by Singleton and Cvetanovic [69] and, within the uncertainty, with the high-temperature determination by Tsuchiya et al. [70].

Other consumption steps for H_2S have not been characterized experimentally. For the reaction of H_2S with HO_2,

$$H_2S + HO_2 \rightleftarrows HS + H_2O_2 \qquad \text{(R6b)}$$

$$H_2S + HO_2 \rightleftarrows HSO + H_2O \qquad \text{(R7)}$$

only a room temperature upper limit has been reported [71]. We have adopted the values for k_6 and k_7, calculated from transition state theory by Zhou et al. [18]. The rate constants for H_2S with O_2 and SO_2 were also drawn from theoretical work of Haynes and coworkers [18,35,36]. For $H_2S + O_2$, we considered in the present work also the spin-forbidden formation of singlet H_2SOO peroxide, followed by the barrierless decomposition path to HSO + OH identified by Montoya et al. [35]. However, the reaction barrier for the initial step is too high for it to be important under the current conditions. Another possibility, as suggested by Starik et al. [72], is that reaction of H_2S with the tiny equilibrium population of singlet oxygen may promote

Table II Selected Reactions from the H_2S Subset. Parameters for use in the Modified Arrhenius Expression $k = AT^{\beta} \exp(-E/[RT])$. Units are mol, cm, s, cal

		A	β	E	Source
1.	$H_2S + M \rightleftarrows S + H_2 + M$	1.6E24	−2.613	89,100	[5]
2.	$H_2S + H \rightleftarrows SH + H_2$	3.5E07	1.940	904	[54]
3.	$H_2S + O \rightleftarrows SH + OH$	7.5E07	1.750	2,900	[55]
4.	$H_2S + O \rightleftarrows HSO + H$	1.4E09	1.100	5,099	[55]
5.	$H_2S + OH \rightleftarrows SH + H_2O$	8.7E13	−0.700	0	[56][a]
		4.1E07	1.770	0	
6.	$SH + H_2O_2 \rightleftarrows H_2S + HO_2$	5.6E04	2.823	8,668	[18][b]
7.	$H_2S + HO_2 \rightleftarrows HSO + H_2O$	1.0E00	3.288	6,224	[18][b]
8.	$SH + HO_2 \rightleftarrows H_2S + O_2$	3.8E04	2.775	−1,529	[18][b]
9.	$H_2S + O_2 \rightleftarrows HSO + OH$	1.0E11	0.000	49,100	[18] est
10.	$H_2S + O_3 \rightleftarrows SO_2 + H_2O$	5.3E08	1.660	11,665	[57]
11.	$H_2S + O_3 \rightleftarrows HOSO + OH$	1.1E03	2.770	11,369	[57]
12.	$H_2S + S \rightleftarrows SH + SH$	7.4E06	2.300	9,007	[58][a,c]
		4.7E07	1.325	−436	[58][d]
13.	$H_2S + SO \rightleftarrows SH + HSO$	5.4E03	3.209	26,824	[18][b]
14.	$H_2S + SO \rightleftarrows SH + HOS$	1.0E13	0.000	36,500	[18] est
15.	$H_2S + SO_2 \rightleftarrows S_2O + H_2O$	1.7E06	1.857	37,740	[36]
16.	$S + H + M \rightleftarrows HS + M$	6.2E16	−0.600	0	[8] est
17.	$S + H_2 \rightleftarrows SH + H$	1.4E14	0.000	19,300	[5]
18.	$SH + O \rightleftarrows SO + H$	4.3E11	0.724	−1,027	[37]
19.	$SH + O \rightleftarrows S + OH$	1.8E12	0.000	0	[37][a]
		4.3E06	2.103	3,583	
20.	$SH + OH \rightleftarrows S + H_2O$	1.0E14	0.000	0	pw, est
21.	$SH + OH \rightleftarrows HOS + H$	1.0E13	0.000	7,400	[18] est
22.	$SH + HO_2 \rightleftarrows HSO + OH$	2.5E08	1.477	−2,169	[18][b]
23.	$SH + HO_2 \rightleftarrows SO + H_2O$	3.2E02	2.579	−2,071	[18][b]
24.	$S + H_2O_2 \rightleftarrows SH + HO_2$	4.1E06	2.200	12,619	[18][b]
25.	$SH + O_2 \rightleftarrows HSO + O$	2.3E06	1.816	20,008	[38]
26.	$SH + O_2 \rightleftarrows S + HO_2$	4.7E06	2.017	36,913	[38]
27.	$SH + O_2 \rightleftarrows SO + OH$	7.5E04	2.052	16,384	[38]
28.	$SH + O_2 \rightleftarrows SO_2 + H$	1.5E05	2.123	11,020	pw
29.	$SH + O_2(+M) \rightleftarrows HSOO(+M)$	8.7E14	−0.260	298	[50]
	Low pressure limit	3.1E19	−0.201	20	
30.	$SH + O_3 \rightleftarrows HSO + O_2$	5.7E12	0.000	556	[59]
31.	$SH + H_2O_2 \rightleftarrows HSOH + OH$	9.5E03	2.800	9,829	[18][b]
32.	$S + OH \rightleftarrows SO + H$	1.5E13	0.191	−1,361	[37]
33.	$S + HO_2 \rightleftarrows SO + OH$	5.7E13	0.000	0	[60]
34.	$S + O_2 \rightleftarrows SO + O$	5.4E05	2.110	−1,450	[61]
35.	$SO + HO_2 \rightleftarrows SO_2 + OH$	1.0E12	0.000	0	pw[e]
36.	$SO + O_2 \rightleftarrows SO_2 + O$	7.6E03	2.370	2,970	[62]
37.	$HSO + O_2 \rightleftarrows SO + HO_2$	6.4E05	2.627	19,013	[18][a]
		2.9E01	3.200	14,529	pw[f]
38.	$HSO + O_2 \rightleftarrows SO_2 + OH$	3.7E01	2.764	6,575	[18]
39.	$HSO + O_2 \rightleftarrows HSO_2 + O$	8.4E–07	5.100	11,312	[18]
40.	$HSO + O_3 \rightleftarrows SH + O_2 + O_2$	1.5E12	0.000	2,230	[59,63]
41.	$HSO + O_3 \rightleftarrows HSO_2 + O_2$	1.3E12	0.000	2,230	[59,63]
42.	$HSO + O_3 \rightleftarrows SO + OH + O_2$	5.0E00	3.630	7,191	pw
43.	$SH + SH(+M) \rightleftarrows HSSH(+M)$	9.0E11	0.155	−1,432	[39][g]
	Low pressure limit:	2.3E31	−4.943	1,998	
	Troe parameters: 1.0 254 2373				
44.	$H_2S + S(+M) \rightleftarrows HSSH(+M)$	6.4E07	1.280	−478	[39]
	Low pressure limit:	2.4E21	−1.612	1,670	

Continued

Table II Continued

		A	β	E	Source
	Troe parameters: 0.5 726 726				
45.	$HSSH + SH \rightleftarrows HSS + H_2S$	6.4E03	2.980	−1,480	[8]
46.	$HSS + H \rightleftarrows H_2S + S$	1.5E08	1.551	2,259	[39][a]
		4.2E18	−1.563	472	
46.	$HSS + H \rightleftarrows SH + SH$	9.7E07	1.620	−1,030	[8,39][a]
		1.6E18	−0.983	261	
47.	$HSS + O_2 \rightleftarrows S_2 + HO_2$	8.4E01	2.950	7,071	pw
48.	$HSS + O_2 \rightleftarrows HSO + SO$	6.6E03	1.900	7,071	pw
49.	$HSS + SH \rightleftarrows S_2 + H_2S$	6.3E03	3.050	−1,105	[8]

[a]Duplicate reaction – the resulting rate constant is the sum of the two expressions.
[b]Calculated from TST.
[c]Abstraction on the triplet surface.
[d]Reaction on the singlet surface. Rate constant is the high-pressure limit.
[e]Reevaluation of the PES indicates that the reaction proceeds without a barrier.
[f]The rate constant for (R37) from Zhou [94] was obtained for quartet transition state. For completeness, we did TST calculations also via the doublet TS.
[g]The high-pressure limit A factor was reduced from the value of 3.5E12 calculated by Zhou et al. [39].

the initiation chemistry; however, this was not investigated in the present work.

The reaction of SH with O_2 is a key step in the oxidation of H_2S at high temperature [62]. It has a significant barrier and attempts to measure the rate coefficient at low temperatures have yielded only upper limits, with a value of 2×10^5 cm^3 mol^{-1} s^{-1} at 298 K from the study of Stachnik and Molina [73] considered to be the most reliable [59]. The reaction, which has been studied theoretically by a number of groups [38,50,55,74–76], has several proposed product channels:

$$SH + O_2 \rightleftarrows HSO + O \quad \text{(R25)}$$

$$SH + O_2 \rightleftarrows S + HO_2 \quad \text{(R26)}$$

$$SH + O_2 \rightleftarrows SO + OH \quad \text{(R27)}$$

$$SH + O_2 \rightleftarrows SO_2 + H \quad \text{(R28)}$$

The theoretical work of Zhou et al. [38] indicated that the reaction proceeds mainly via a four-membered cyclic transition state to form SO + OH (R27) at temperatures below 1000 K, whereas HSO + O (R25) becomes the major product channel above this temperature. However, Garrido et al. [75] identified a new and faster reaction path to form SO_2 + H (R26) via a three-center ring structure.

The existence of the new pathway is supported by the recent theoretical study of Freitas et al. [76]. They characterized a transition state leading from HSOO via an electronically excited state to HSO_2, with a CCSD(T) energy extrapolated to the complete basis set limit of 19.8 kcal mol^{-1} above HSOO. Assuming this is the bottleneck, SH + O_2 collisions will maintain a small equilibrium population of HSOO, which lies 6.4 kcal mol^{-1} below SH + O_2 [77]. Accordingly, we evaluated the bimolecular TST for SH + O_2 → products via this TS with a barrier of 13.4 kcal mol^{-1}. Because HSO_2 is formed with energies E of about 82 kcal mol^{-1} or more, well above the S–H dissociation threshold E_0 of about 21 kcal mol^{-1} [75], we assume the major products are H + SO_2 (see Table II). We justify this via evaluation of the microcanonical TST result $k(\mathrm{E}) = G^{\ddagger}(E - E_0)/(h\,N(E))$ for first-order dissociation of nascent vibrationally excited HSO_2. $N(E)$ is the density of states for HSO_2, and $G^{\ddagger}(E - E_0)$ is the sum of states for the TS for HSO_2 dissociation to H + SO_2. This yields $k(E) = 1.6 \times 10^{14}$ s^{-1}, three orders of magnitude faster than collisional stabilization at 100 atm pressure.

Figure 2 shows an Arrhenius plot for the SH + O_2 reaction. Tsuchiya et al. [62] derived the rate constant from measured concentration profiles of H and O atoms in flash-photolysis/shock tube experiments of H_2S/O_2/Ar mixtures. They could not identify the major product channel with certainty, but in their analysis they assumed formation of HSO + O. The theoretical values derived by Zhou et al. [38] and Garrido et al. [75] are all consistent with the room temperature upper limit by Stachnik and Molina [73] but also

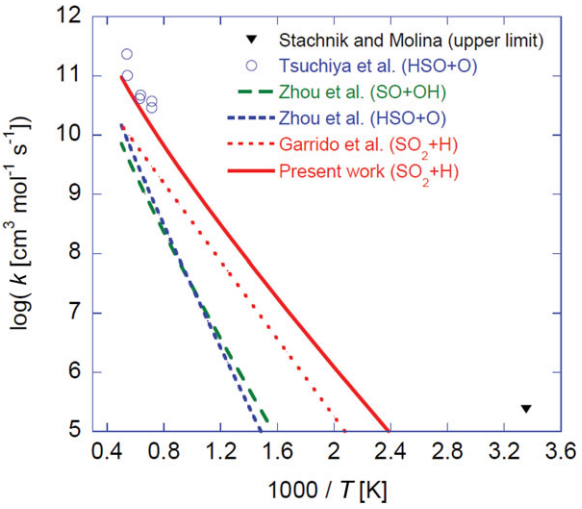

Figure 2 Arrhenius plot for the SH + O_2 reaction. Experimental values are shown as symbols, whereas curves denote rate constants derived from theory. Sources: Stachnik and Molina [73], Tsuchiya et al. [62], Zhou et al. [38], and Garrido et al. [75].

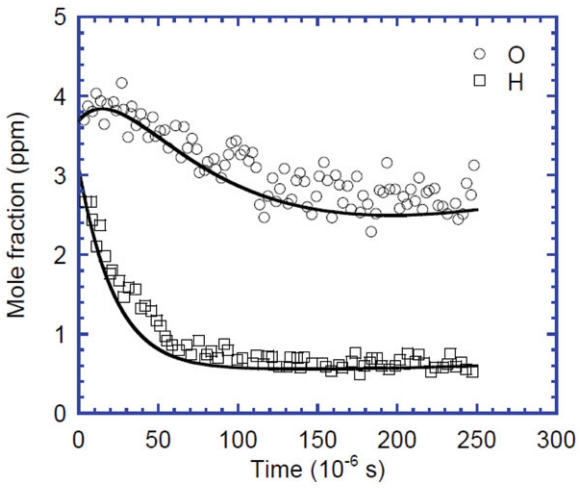

Figure 3 Concentration profiles of O and H atoms after laser photolysis behind a reflected shock wave. Symbols denote experimental results from Tsuchiya et al. [62], whereas curves denote predictions with the chemical kinetic model of the present work. Conditions: $T = 1398$ K, $P = 1.54$ atm, 51 ppm H_2S, 3050 ppm O_2, atomic O and H formed in flash pyrolysis; balance Ar.

well below the values derived by Tsuchiya et al. The present rate constant for the dominating product channel to SO_2 + H is almost an order of magnitude higher than the value of Garrido et al., used in the modeling study of Zhou et al. [18].

The apparent agreement of the present rate constant with the values of Tsuchiya et al. is fortuitous since they assumed HSO + O to be the major product channel. Actually, Tsuchiya et al. concluded based on their measurements that SO_2 + H was unlikely to be the major product channel for SH + O_2. To resolve this issue, we used the present kinetic model to reinterpret selected data from Tsuchiya et al. (Fig. 3). The comparison shows that the present rate constants and product channels for SH + O_2 are consistent with their measurements. In fact, the present model predictions of H and O show only a limited sensitivity to the rate constant for the SH + O_2 reaction.

At the low to medium temperature, high-pressure conditions of the present work, it is of interest whether an adduct formed from SH + O_2 may have a sufficient lifetime to react. Theoretical studies [38,50,55,75,76] indicate that the thiylperoxyl radical (HSOO) is formed from recombination of SH and O_2,

$$\mathrm{SH + O_2(+M) \rightleftarrows HSOO(+M)} \qquad \text{(R29)}$$

whereas formation of HSO_2 or HOSO is inaccessible. Turnipseed et al. [78] proposed that reaction (R29) could be partially equilibrated in the atmosphere, with subsequent reactions of with HSOO promoting oxidation of SH. Goumri et al. [50] and Zhou et al. [38] found (R29) to be essentially barrierless, whereas Resende and Ornellas [74] and Ballester and Varandas [79] found barriers of 12 and 8 kcal mol^{-1}, respectively. The difference may partly be attributed to the different geometries of HSOO that are separated by only about 1 kcal mol^{-1} in energy [75]. The recent study by Garrido et al. [75] calculated a 7 kcal mol^{-1} barrier to formation of *cis*-HSOO, whereas formation of a skewed HSOO isomer proceeds without a barrier.

The HSOO adduct is weakly bound, and the reaction is rapidly equilibrated. This means that the concentration of HSOO will remain very low, even at the pressures of the present study. Dissociation of HSOO to HSO + O has a significant barrier and is not competitive. However, a fast reaction of HSOO and O_2 (the only abundant reactant under our conditions) could possibly be important,

$$\mathrm{HSOO + O_2 \rightleftarrows HSO + O_3}$$

There are no data for this step in the literature, but the reverse reaction, HSO + O_3, has been studied experimentally at low temperatures [63,80–82]. The reaction apparently has two major product channels,

$$\mathrm{HSO + O_3 \rightleftarrows SH + O_2 + O_2} \qquad \text{(R40)}$$

$$HSO + O_3 \rightleftarrows HSO_2 + O_2, \qquad (R41)$$

with a branching fraction reported to be roughly 50% at 298 K [59]. Conceivably, the $SH + O_2 + O_2$ channel (R40) is a sequence of the two steps,

$$HSO + O_3 \rightleftarrows HSOO + O_2$$

$$HSOO(+M) \rightleftarrows SH + O_2(+M) \qquad (R29b)$$

since HSOO decomposes readily even at 298 K. Taking both steps in the reverse direction, we get the sequence $SH \xrightarrow{+O_2} HSOO \xrightarrow{+O_2} HSO + O_3$, which could conceivably be important under the conditions of our work. In the reaction mechanism, we have adopted the one-step reaction (R40), as recommended by Atkinson et al. [59]. However, owing to the fast equilibration of (R29), modeling predictions are not sensitive to whether (R40) is put in as a single reaction or divided into two steps.

Consequently, $SH + O_2 + O_2 \rightarrow HSO + O_3$ (R40b) may be a source of ozone under the conditions of the present work. Ozone is much more reactive than molecular oxygen and may promote reaction. Following other recent studies on low-temperature sulfur chemistry [83,84], we include an O_3 reaction subset with rate constants mostly from Atkinson et al. [59]. Ozone may interact with the O/H radical pool or react with sulfur species, primarily H_2S or SH. The $H_2S + O_3$ reaction has been studied both experimentally [85–91] and theoretically [57]. Experimental work [88–90] indicates that the overall reaction is complex, involving a radical-forming initial step followed, after an induction time, by a free radical mechanism. Reaction orders of 0–0.5 in H_2S and 1.5 in O_3 have been reported [86,87,89,90]. The reaction appears to be sensitive to surfaces, and reported results show a considerable scatter.

The most reliable measurement of $H_2S + O_3$ is believed to be the room temperature upper limit by Becker et al. [88]. The recent theoretical study by Mousavipour et al. [57] indicates that $SO_2 + H_2O$ (R10) is the dominating product channel for $H_2S + O_3$, along with a (very) minor channel forming HOSO + OH (R11). We have tentatively adopted the rate constants from Mousavipour et al., even though the suggestion of (R10) as the dominant channel seems to be inconsistent with the experimental observations.

The rate constant for $SH + O_3$ (R30) has been measured at low temperature [80,82,92], and values are in good agreement, indicating a fast reaction with a low activation energy. We have adopted the recommendation by Atkinson et al. [59]. The recent theoretical study by Resende and Ornellas [93] indicates a significantly higher barrier to reaction than derived from experiment. However, this is contradicted by our own preliminary analysis and more work is desirable on this reaction.

Owing to the low reactivity of the SH radical, the SH + SH reaction becomes important, even at oxidizing conditions. This reaction has two major product channels:

$$SH + SH \rightleftarrows H_2S + S \qquad (R12b)$$

$$SH + SH(+M) \rightleftarrows HSSH(+M) \qquad (R43)$$

The rate constant for the $H_2S + S$ reaction (R12), which is believed to be largely independent of pressure, was taken from the combined experimental and theoretical study of Gao et al. [58]. The high- and low-pressure limits, as well as the falloff behavior, for the SH + SH recombination step (R43) were initially drawn from the RRKM study of Zhou et al. [39]. However, for this reaction rate parameters are more uncertain, since extrapolation is required. In the present work, we modified the high-pressure limit $k_{43,\infty}$ to improve agreement with experiment under stoichiometric conditions. This is discussed in more detail below. The reaction feeds into the S_2H_x subset, which was drawn largely from Haynes and coworkers [8,39].

Reactions of sulfur radicals with O_2 can be important for the generation of chain carriers, even under conditions with fairly low concentrations of oxygen. In addition to $SH + O_2$ discussed above, reactions of HSO, SO, S, and HSS with O_2 should be considered. The rate constants for the chain branching steps $SO + O_2$ and $S + O_2$ are well established [83,84], but values for $HSO + O_2$ and $HSS + O_2$ are more uncertain.

For $HSO + O_2$, the only reliable measurement is a room temperature upper limit of 1.2×10^7 cm^3 mol^{-1} s^{-1} from Lovejoy et al. [81]. The reaction has several possible product channels,

$$HSO + O_2 \rightleftarrows SO + HO_2 \qquad (R37)$$

$$HSO + O_2 \rightleftarrows SO_2 + OH \qquad (R38)$$

$$HSO + O_2 \rightleftarrows HSO_2 + O \qquad (R39)$$

According to theoretical work, the fastest channel is (R38) [18], whereas (R39) is quite slow [46]. However, also (R37) has a significant impact on the system,

Table III Experimental Conditions for the H_2S Oxidation Study

Experiment	Inlet Composition[a,b]	Pressure (bar)	Temperature (K)	Residence Time[c] (s)	Reactor
1	756 ppm H_2, 1290 ppm O_2; N_2 ($\phi = 0.88$)	30	450–900	3,520/T (K)	Quartz
2	750 ppm H_2, 1190 ppm O_2; CO_2 ($\phi = 0.94$)	30	450–900	3,520/T (K)	Quartz
3	801 ppm H_2, 43600 ppm O_2; N_2 ($\phi = 0.028$)	30	450–900	3,520/T (K)	Quartz
4	806 ppm H_2, 42300 ppm O_2; N_2 ($\phi = 0.029$)	100	450–900	11,700/T (K)	Quartz
5	802 ppm H_2, 40100 ppm O_2; N_2 ($\phi = 0.029$)	100	450–900	6,610/T (K)	Alumina

[a]Volume basis; balance N_2 or CO_2.
[b]The fuel air equivalence ratio ϕ is based on the overall reaction $H_2S + 1.5O_2 = SO_2 + H_2O$.
[c]The nominal residence time in the isothermal region of the reactor. It is a function of temperature, since the mass flow rate was held constant.

because the subsequent reaction of SO with O_2 leads to formation of atomic oxygen.

Prior investigations of HSO chemistry with O_2 relied on G3 energies at CASSCF geometries [94]. Investigation of the HSO + O_2 transition states using CBS-QB3 theory leads to differences in the rate constants of up to a factor of 10. This is consistent with the target energy accuracies of G3 and CBS-QB3 theory for stable species, and we provisionally suggest uncertainties in these reaction barriers of ca. 2.5 kcal mol^{-1}, which corresponds roughly to an order of magnitude in the rate constant.

For HSS + O_2, the original energy calculations were based on MP2/6-31G(d) geometries [18]. We reevaluated the TSs using B3LYP/6-311G(2d,d,p) theory, followed by CBS-QB3 for single-point energies. Based on this, for the doublet TS for HSS + O_2 → HSO + SO, we get a barrier of 39.2 kcal mol^{-1}, and for the two quartet TSs that we attribute to HSS + O_2 → S_2 + HO_2, we get 18.1 and 10.7 kcal mol^{-1}, respectively. In addition, we identified a new doublet TS for HSS + O_2 → S_2 + HO_2 with a barrier of 8.7 kcal mol^{-1}. For this lowest barrier pathway, our TST calculation (including Eckart tunneling and a hindered rotor) yields a rate constant which is about an order of magnitude faster than the previous estimate.

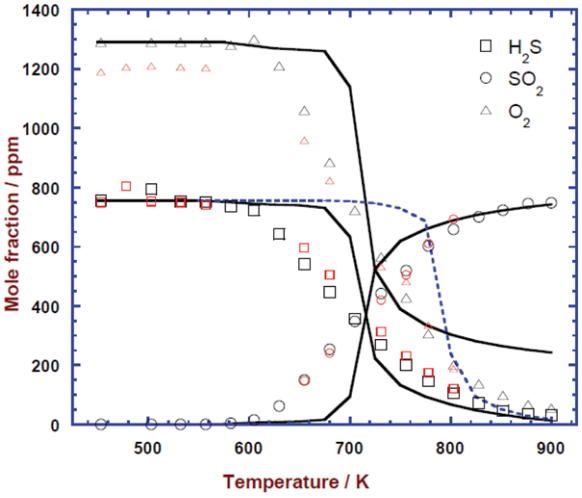

Figure 4 Comparison of experimental data and modeling predictions for H_2S oxidation under stoichiometric conditions at 30 bar. Experimental data are shown as symbols, modeling predictions as solid lines. The dashed line denotes predictions with the original value of $k_{43,\infty}$ (SH + SH (+M) ⇌ HSSH (+M)) from Zhou et al. [39]. Inlet composition: 756 ppm H_2S, 1290 ppm O_2, balance N_2 ($\phi = 0.88$, black symbols) or 750 ppm H_2S, 1190 ppm O_2, balance CO_2 ($\phi = 0.94$, smaller red symbols). The residence time in the isothermal zone is calculated from τ (s) = 3520/T (K).

RESULTS AND DISCUSSION

Experiments for H_2S oxidation with high dilution in N_2 (or CO_2) as a function of temperature from 450 to 900 K were conducted under stoichiometric and oxidizing conditions. Table III lists the experimental conditions. The fuel–air equivalence ratio ϕ ranged from 0.9 to 0.03. In the following, the experimental results are compared with modeling predictions. Calculations shown in the figures, conducted using the CHEMKIN PRO software package [95], were restricted to the isothermal zone. Simulations with the full measured temperature profile were similar.

Figure 4 shows results for H_2S oxidation under stoichiometric conditions and a pressure of 30 bar with both N_2 and CO_2 as carrier gas. Symbols denote the experimental data, and lines denote numerical results. The onset temperature of the reaction is approximately 625 K. Above this temperature, the degree of conversion increases gradually with temperature; at the highest temperature of 900 K, 30 ppm H_2S and 50 ppm O_2 are still unreacted. The experimental results in CO_2 agree well with those in N_2, showing that the CO_2 has a little effect on the experiment results under these

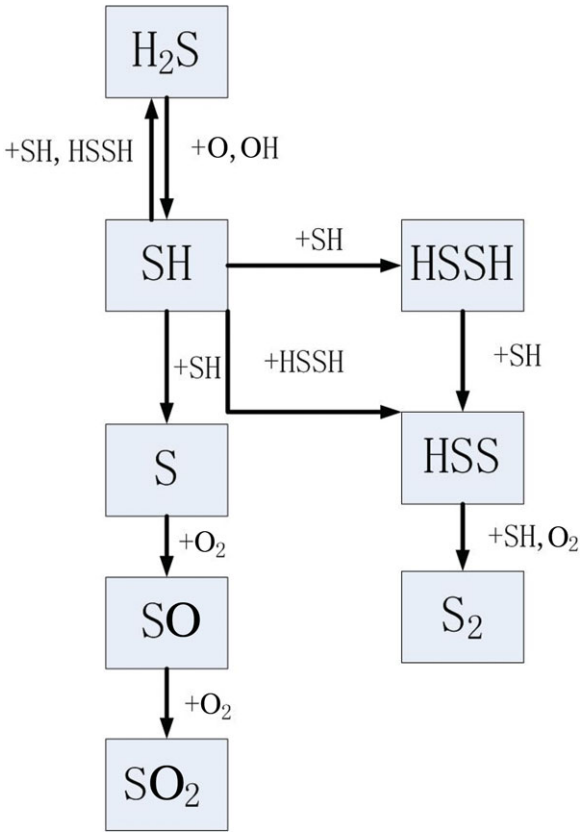

Figure 5 Pathway diagram for H_2S under stoichiometric conditions (corresponding to Fig. 4) and 700 K.

conditions. This is expected, since interaction of CO_2 with the O/H radical pool [96] or with sulfur radicals would be expected to occur only at higher temperatures than those of the present study.

Two sets of modeling predictions are shown. The solid lines denote calculations with the basis mechanism. In this mechanism, we reduced the *A* factor of the high-pressure limit for SH + SH (+M) ⇄ HSSH (+M) (R43) by a factor of four to improve agreement with experiment. This change is considered to be within the uncertainty in the high-pressure limit, for which there are no experimental results. The dashed line shows predictions using the value of $k_{43,\infty}$ calculated by Zhou et al. [39], resulting in a shift upwards in the temperature for onset of reaction of about 100 K.

The modification of $k_{43,\infty}$ allows a satisfactory prediction of the temperature for 50% conversion of H_2S. Still, important differences are seen when comparing experimental results and modeling predictions. Most importantly, the temperature for onset of reaction is overpredicted; the calculations indicate a steeper gradient in the H_2S concentration profile than observed.

Figure 5 shows a reaction path diagram for H_2S oxidation at 700 K and stoichiometric conditions, corresponding to Fig. 4. Hydrogen sulfide is consumed by reaction with the O/H radical pool (R3, R5) to form SH. The SH radical is largely consumed by its self-reaction, forming either H_2S + S (R12b) or HSSH (R43). The atomic S is oxidized to SO_2 in the chain-branching sequence S + O_2 → SO + O (R34), SO + O_2 → SO_2 + O (R36). HSSH, on the other hand, is oxidized to S_2 through the sequence HSSH + SH → HSS + H_2S (R45), HSS + SH → S_2 + H_2S (R49), and HSS + O_2 → S_2 + HO_2 (R47). According to the current calculations, formation of oxidized sulfur species from the H_xS_2 is very limited under these conditions.

Figure 6 shows sensitivity coefficients for H_2S under the same conditions (stoichiometric, 700 K). The analysis shows that the predicted H_2S concentration is mainly sensitive to the branching fraction for the SH + SH reaction. Formation of H_2S + S (R12b) strongly promotes the oxidation rate due to the subsequent chain-branching reactions of S and SO with O_2 (R34, R36), whereas formation of HSSH (R43) is chain terminating. None of the reactions in the S_2 subset is seen to promote oxidation; predictions, however, are sensitive to the terminating steps H_2S + S (R44) and HSS + SH (R49). We attribute the discrepancy between experimental results and modeling predictions mostly to uncertainties in the S_2 chemistry.

Figure 7 shows results under oxidizing condition at 30 bar pressure. The initiation temperature is 520 K, approximately 100 K lower than at stoichiometric conditions. Contrary to the behavior in Fig. 4, the concentration gradient of H_2S with respect to temperature is steep and full oxidation to SO_2 is obtained already at 575 K. This indicates that a strong chain-branching mechanism is active already at low temperature.

The model (solid lines) predicts a significantly higher temperature for onset of reaction, about 625 K. However, the concentration profiles are similar to those observed experimentally, just shifted 100 K to higher temperatures. The dashed line shows predictions conducted with the H_2S + O_3 reaction (R10, R11) omitted. Reaction (R10), which is the dominating product channel, serves in effect as a chain-terminating step because it takes out reactive ozone without providing chain carriers. Omission of this step serves to bring the predicted onset temperature in closer accordance with observations. However, this change causes a smaller gradient in H_2S than observed above the onset temperature and leads to an underestimation of SO_2, caused by prediction of significant amounts of SO_3.

Figure 8 shows results under oxidizing condition at 100 bar. The larger black symbols represent experimental results conducted in a quartz tube, whereas the smaller red symbols denote data obtained in an

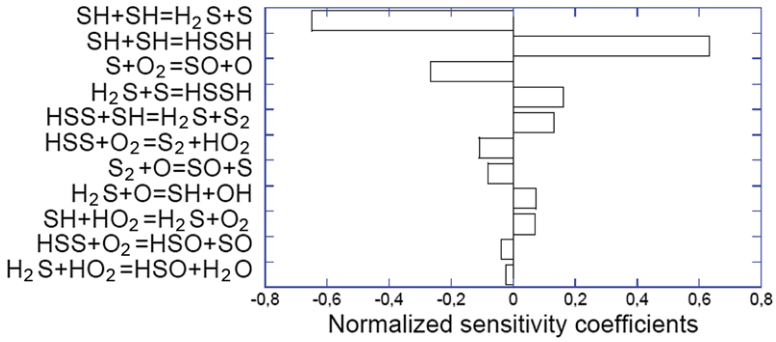

Figure 6 Sensitivity coefficients for H_2S under stoichiometric conditions (corresponding to Fig. 4) and 700 K.

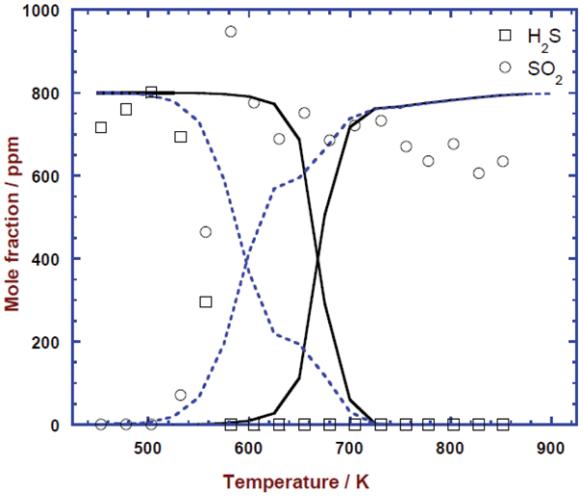

Figure 7 Comparison of experimental data and modeling predictions for H_2S oxidation under oxidizing conditions at 30 bar. Experimental data are shown as symbols, modeling predictions as solid lines. The dashed line denotes predictions omitting the $H_2S + O_3$ reaction (R10, R11). Inlet composition: 801 ppm H_2S, 4.4% O_2, balance N_2 ($\phi = 0.028$). The residence time in the isothermal zone was τ (s) $= 3100/T$ (K).

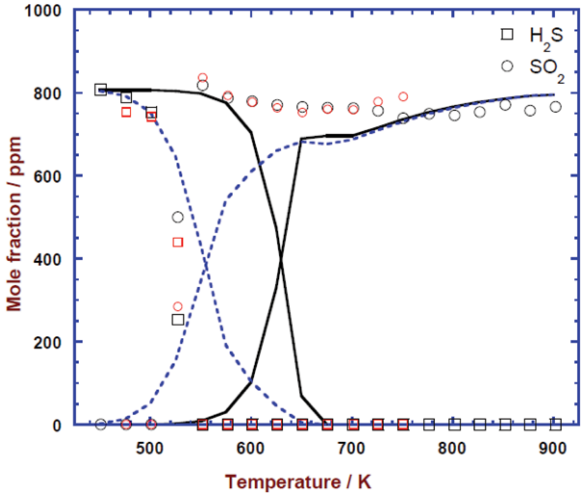

Figure 8 Comparison of experimental data and modeling predictions for H_2S oxidation under oxidizing conditions at 100 bar. Experimental data were obtained in a quartz (black symbols) and an alumina (smaller red symbols) reactor, respectively. Modeling predictions are shown as solid lines. The dashed line denotes predictions omitting the $H_2S + O_3$ reaction (R10, R11). Inlet composition: 806 ppm H_2S, 4.2% O_2, balance N_2 ($\phi = 0.029$). The residence time in the isothermal zone is calculated from τ (s) $= 10{,}330/T$ (K) for the quartz tube and τ (s) $= 6610/T$ (K) for the alumina tube.

alumina tube. The hydrogen sulfide oxidation is initiated at around 475 K and completed at 550 K. The earlier onset, compared to data at 30 bar, is partly caused by a longer residence time at 100 bar. The behavior is similar to that at 30 bar, except that the initiation temperature is shifted to lower values.

Despite some deviation in residence time, the experimental results from the alumina tube agree well with those of the quartz tube. This is an indication that surface effects, if present, are of minor significance under the conditions with high pressure. This issue is discussed further below.

The modeling results show deviations similar to those at 30 bar. Again, the full model overpredicts the onset temperature. Omission of (R10) serves to reduce the predicted onset temperature significantly but reduces also the H_2S concentration gradient and the SO_2 level.

Figure 9 shows a reaction path diagram for H_2S oxidation at 600 K and oxidizing conditions, corresponding to Fig. 8. Oxidation paths are very different from those under stoichiometric conditions. A major fraction of the hydrogen sulfide is consumed by reaction with ozone (R10) to form SO_2 directly. A similar amount reacts with O/H radicals (R5, R6b) to form SH, which is consumed by reaction with two oxygen

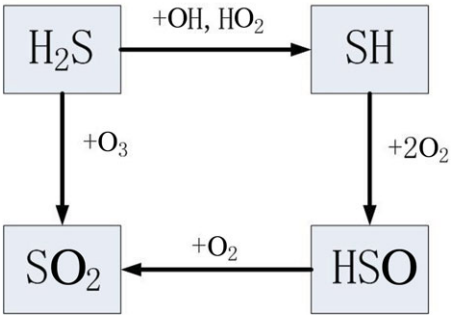

Figure 9 Pathway diagram for H_2S under oxidizing conditions (corresponding to Fig. 8) and 600 K.

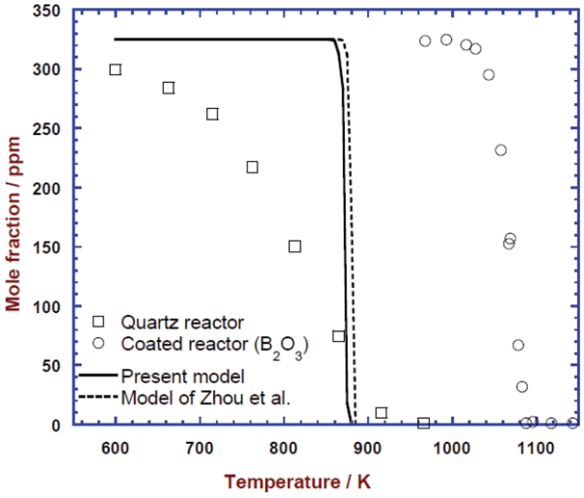

Figure 11 Comparison of modeling predictions for H_2S oxidation with the flow reactor results from Zhou et al. [18]. The experiments were conducted in an uncoated and a coated (B_2O_3) quartz reactor at atmospheric pressure. Inlet composition: 325 ppm H_2S, 600 ppm O_2, balance N_2. The residence time in the isothermal zone was 0.2 s.

molecules (R40b), yielding HSO and O_3. The HSO reacts mostly with O_2 to form SO_2. Owing to the high oxygen concentrations, S_2 species are only formed in minor amounts.

Figure 10 shows sensitivity coefficients for H_2S under lean conditions (100 bar, 600 K). The analysis shows that consumption of H_2S is promoted by chain-propagating or -branching reactions, primarily $H_2S + HO_2$ (R6b), $HSO + O_2$ (R38), and $H_2S + O$ (R4). Even though it consumes H_2S, the $H_2S + O_3 \rightarrow SO_2 + H_2O$ (R10) is a major inhibiting step because it forms stable products. It competes with the minor radical producing channel HOSO + OH (R11), which has a negative sensitivity coefficient.

It is known that oxidation of H_2S is sensitive to surface reactions, and it is important to assess whether heterogeneous effects can explain some of the differences between measurements and modeling predictions under the present conditions. Adesina et al. [9] report that for thermolysis of hydrogen sulfide (i.e., under oxygen-free conditions) there are no indications of surface effects on quartz at 1073 K. However, under oxidizing conditions significant heterogeneous effects have been reported. An increase of the surface to volume ratio in glass reactors serves to inhibit H_2S oxidation and explosion at low pressure and temperatures of 500–600 K [13,14]. Under these conditions, the main impact of the surface seems to be to remove chain carriers, while surface initiation involving a reaction between H_2S and O_2 is less important. More recently, Zhou et al. [18,94,100] investigated the impact of surface effects on H_2S oxidation in quartz flow reactors at atmospheric pressure. They found that a 30-fold increase in the surface area of the reactor slightly enhanced H_2S consumption in the 650–950 K range, while it inhibited formation of H_2 [94,100]. With a B_2O_3 coating of the quartz surface, the system became much less reactive [18,94,100].

Figure 11 compares modeling predictions with the experimental data of Zhou et al. [18], obtained with

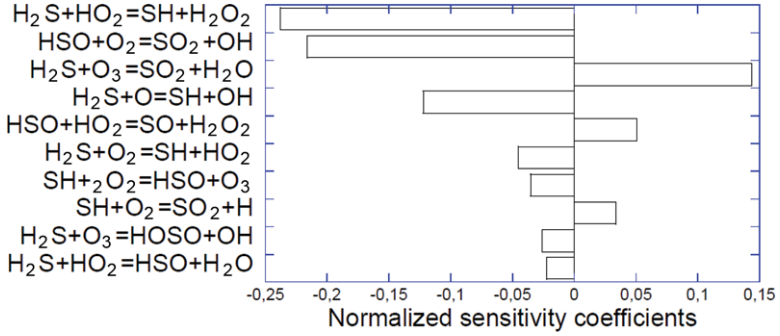

Figure 10 Sensitivity coefficients for H_2S under oxidizing conditions (corresponding to Fig. 8) and 600 K.

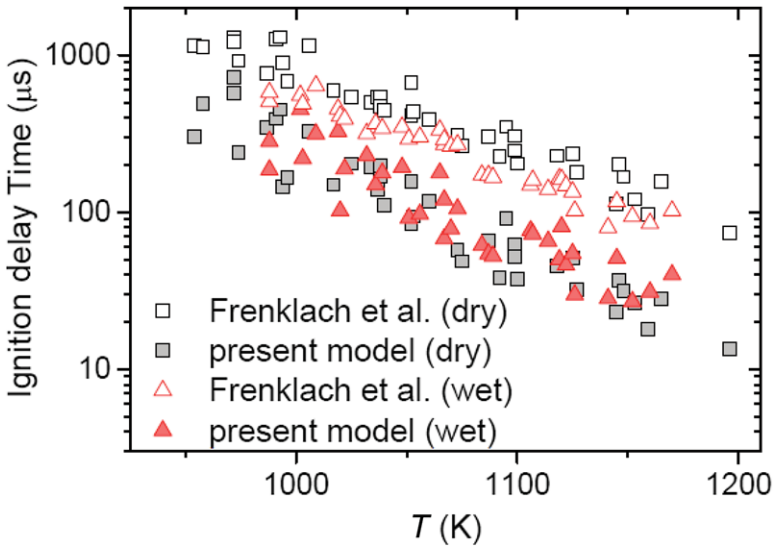

Figure 12 Ignition delay time of H_2S/air (4–22% H_2S, 16–20% O_2) and H_2S/H_2O/air (4–21% H_2S, 2–13% H_2O) mixtures versus temperature. Pressure was varied between 29 and 47 atm, whereas the equivalence ratio ϕ changed from 0.3 to 2. Open symbols present experimental data from Frenklach et al. [19], whereas the closed symbols are the results of the present simulations.

and without coating of the quartz reactor surface. The pressure is lower, but the temperature range and composition are comparable to those of the present work. The figure illustrates the considerable impact of the surface condition. Two sets of predictions are shown, conducted with the present model (solid lines) as well as with the basis mechanism of Zhou et al. [18] (dashed lines). Under these conditions, the two mechanisms result in very similar concentration profiles for H_2S. Both models predict the sharp onset of reaction observed in the coated reactor, but the calculated onset temperature is closer to that reported for the uncoated reactor.

Surfaces may initiate reaction and promote oxidation by catalyzing fuel conversion or inhibit oxidation by acting as a sink for radicals. The difference between the impact of the quartz surface between the batch and flow reactor experiments may be attributed to differences in temperature and pressure that could change the balance between surface initiation/oxidation and loss of radicals on the wall. Based on the available results, we believe that the impact of heterogeneous reactions in the high-pressure quartz reactor used in the present work is limited. This is supported by the agreement between results obtained in the quartz and alumina reactors.

To extend the evaluation of the present model, predictions are compared also to selected data obtained at high temperature and pressure in shock tubes. Figure 12 shows data from Frenklach et al. [19] on ignition delays of H_2S in air, with and without presence of water vapor. The experiments were conducted at 34 bar and temperatures in the range 950–1200 K. The present model underestimates the ignition delays by factors of 2–6, most pronounced under dry conditions and at high temperatures.

Figure 13 shows the results of a sensitivity analysis for the ignition delay time under typical conditions (12% H_2S in air, 38 bar, and 1060 K). The sensitivity coefficients are calculated as $(\Delta\tau/\tau)/\Delta k/k)$, so a negative coefficient indicates a promoting effect. Similar to the flow reactor results, the modeling predictions are very sensitive to the branching fraction for the SH + SH reaction. Formation of H_2S + S (R12b) strongly promotes the oxidation rate due to the subsequent chain-branching reactions of S and SO with O_2 (R34, R36) while formation of HSSH (R43) is chain terminating. Also a number of the reactions in the S_2 subset, such as the terminating steps H_2S + S (R44) and HSS + SH (R49), show significant sensitivity coefficients. No attempt was made to improve modeling predictions for these conditions; further work is desirable to reduce uncertainties in the S_2 chemistry subset.

Figure 14 compares modeling predictions with ignition delay data from Mathieu et al. [20] for mixtures of H_2 and H_2S, obtained at pressures of about 34 atm and 1045–1860 K. Under these conditions, the radical pool is determined to a larger extend by the H_2/O_2 subset of the mechanism, and the agreement with experiment is better than for the conditions of Frenklach et al.

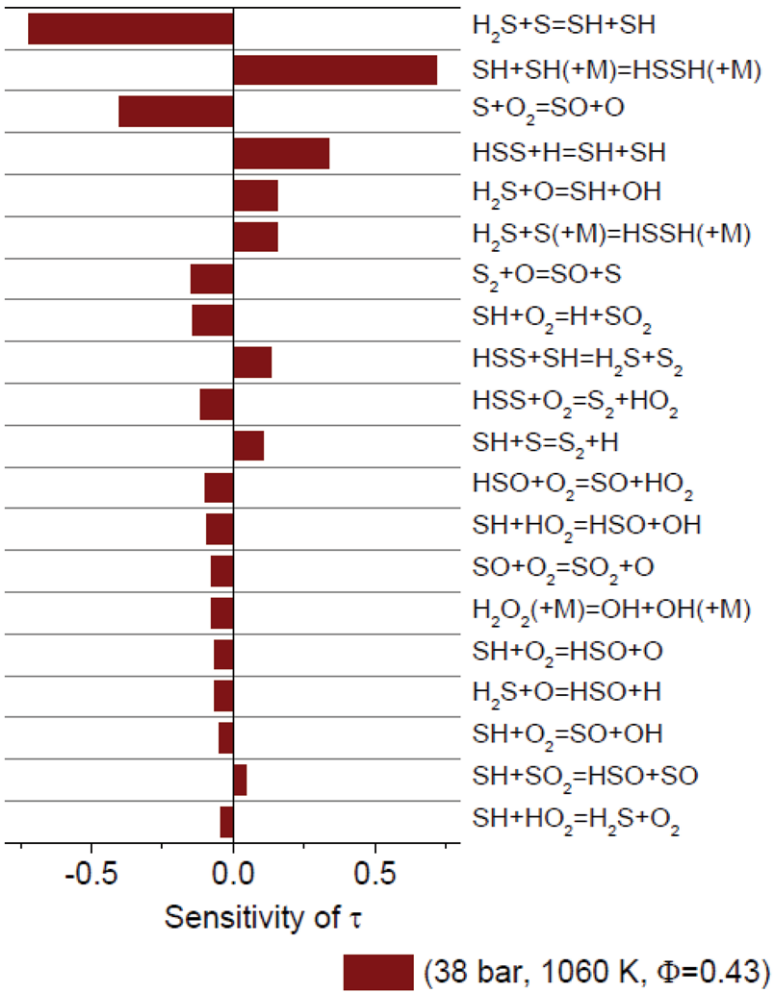

Figure 13 Sensitivity of ignition delay time to the reaction rate constants (corresponding to Fig. 8). Results are shown for 12% H_2S mixed with air ($\phi = 0.43$) at 38 bar and 1060 K.

(Fig. 12). For low concentrations of H_2S (100 and 400 ppm), the predictions compare well to the measurements, but the model systematically underpredicts the ignition delays for higher concentrations of H_2S (1600 ppm).

CONCLUSIONS

Hydrogen sulfide oxidation experiments were conducted at high pressure (30 and 100 bar) under oxidizing and stoichiometric conditions, respectively, and temperatures ranging from 450 to 925 K. The H_2S oxidation behavior depended strongly on the stoichiometry. Under stoichiometric conditions, the oxidation of H_2S was initiated at 600 K, with the consumption rate increasing only slowly with temperature up to 900 K. Under oxidizing conditions, the onset temperature for reaction was 500–550 K, depending on pressure and residence time, with a steep gradient in H_2S above this temperature. The data were interpreted in terms of a detailed chemical kinetic model. The rate constants for selected reactions, including $SH + O_2 \rightleftarrows SO_2 + H$, were determined from ab initio calculations. Modeling predictions generally overpredicted the temperature for onset of reaction. Calculations were sensitive to reactions of the comparatively unreactive SH radical. Under stoichiometric conditions, the oxidation rate was mostly controlled by the SH + SH branching ratio to form $H_2S + S$ (promoting reaction) and HSSH (terminating). Further work is desirable on the SH + SH recombination and on subsequent reactions in the S_2 subset of the mechanism. Under oxidizing conditions, a high O_2 concentration (augmented by the high pressure) causes the reaction $SH + O_2 + O_2 \rightarrow HSO + O_3$ to become the major consumption step for SH,

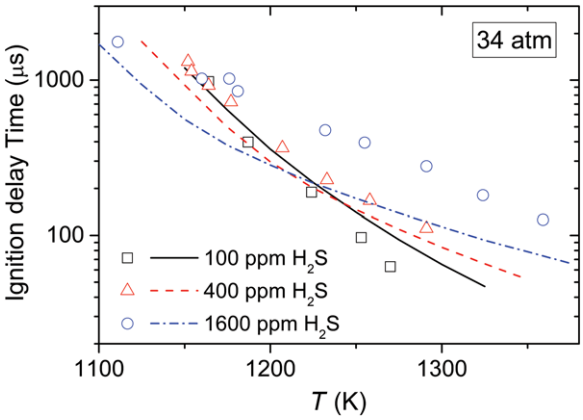

Figure 14 Ignition delay time of $H_2S/H_2/O_2/Ar$ mixtures ($\phi = 0.50$–0.58) versus temperature. The H_2S concentrations are 100, 400, and 1600 ppm, respectively, with 1% H_2 and 1% O_2. Symbols denote experimental data from Mathieu et al. [20], whereas lines represent simulations conducted at the average pressure of 34.1 atm.

according to the model. Consequently, calculations become very sensitive to the rate constant and product channels for the $H_2S + O_3$ reaction, which are currently not well established.

The work is part of the CHEC (Combustion and Harmful Emission Control) research program at DTU Chemical Engineering. YS wishes to acknowledge funding from CSC (China Scholarship Council). PM thanks the R. A. Welch Foundation (grant B-1174) for support.

BIBLIOGRAPHY

1. Raymond, M. E. D. Hydrocarbon Proc July, 1975, 139–142.
2. Towler, G. P.; Lynn, S. Ind Eng Chem Res 1993, 32, 2800–2811.
3. Kaloidas, V.; Papayannakos, N. Chem Eng Sci 1989, 44, 2493–2500.
4. Harvey, W. S.; Davidson, J. H.; Fletcher, E. A. Ind Eng Chem Res 1998, 37, 2323–2332.
5. Shiina, H.; Miyoshi, A.; Matsui, H. J Phys Chem A 1998, 102, 3556–3559.
6. Karan, K.; Mehrotra, A. K.; Behic, L. A. AIChE J 1999, 45, 383–389.
7. Hawboldt, K. A.; Monnery, W. D.; Svrcek, W. Y. Chem Eng Sci 2000, 55, 957–966.
8. Sendt, K.; Jazbec, M.; Haynes, B. S. Proc Combust Inst 2002, 29, 2439–2446.
9. Adesina, A. A.; Meeyoo, V.; Foulds, G. J Hydrogen Energy 1995, 20, 777–783.
10. Binoist, M.; Labegorre, B.; Monnet, F.; Clark, P. D.; Dowling, N. I.; Huang, M.; Archambault, D.; Plasari, E.; Marquaire, P.-M. Ind Eng Chem Res 2003, 42, 3943–3951.
11. Wilson, C.; Hirst, D. M. Prog React Kinet 1996, 21, 69–132.
12. Cullis, C. F.; Mulcahy, M. F. R. Combust Flame 1972, 18, 225–292.
13. Thompson, H. W.; Kelland, N. S. J Chem Soc 1931, 1809–1827.
14. Farkas, L. Z Elektrochem 1931, 37, 670–673.
15. Davies, D. A.; Walsh, A. D. Proc Combust Inst 1974, 14, 475–483.
16. Gray, P.; Sherrington, M. E. J Chem Soc, Faraday Trans 1 1974, 70, 2338.
17. Pahl, R.; Holtappels, K. Chem Eng Technol 2005, 28, 746–749.
18. Zhou, C.; Sendt, K.; Haynes, B. S. Proc Combust Inst 2013, 34, 625–632.
19. Frenklach, M.; Lee, J. H.; White, J. N.; Gardiner, W. C., Jr. Combust Flame 1981, 41, 1–16.
20. Mathieu, O.; Deguillaume, F.; Petersen, E. L. Combust Flame 2014, 161, 23–36.
21. Chamberlin, D. S.; Clarke, D. R. Ind Eng Chem Res 1928, 20, 1016–1018.
22. Cohen, L. Fuel 1955, 34, S119–S122.
23. Gibbs, G. J.; Calcote, H. F. J Chem Eng Data 1959, 4, 226–237.
24. Flockenhaus, C. Gas Wärme Int 1969, 18, 153–156.
25. Levy, A.; Merryman, E. L. Combust Flame 1965, 9, 229–240.
26. Merryman, E. L.; Levy, A. J Air Poll Assoc 1967, 17, 800.
27. Sachyan, G. A.; Gershenzon, Yu. M.; Nalbandyan, A. B. Dokl Akad Nauk SSSR 1967, 175, 1378.
28. Merryman, E. L.; Levy, A. Proc Combust Inst 1970, 13, 427–436.
29. Selim, H.; Al Shoaibi, A.; Gupta, A. K. Appl Energy 2011, 88, 2601–2611.
30. Selim, H.; Gupta, A. K.; Al Shoaibi, A. Appl Energy 2012, 98, 53–58.
31. Selim, H.; Ibrahim, S.; Al Shoaibi, A.; Gupta, A. K. Appl Energy 2013, 109, 119–124.
32. Selim, H.; Ibrahim, S.; Al Shoaibi, A.; Gupta, A. K. Appl Energy 2014, 113, 1134–1140.
33. Tesner, P. A.; Rubinov, R. Kh.; Sherov, I.Sh. Gaz Prom 1984, 9, 29–30.
34. Chernysheva, A. V.; Basevich, V. Ya.; Vedeneev, V. I.; Arutyunov, V. S. Bull Acad Sci USSR 1991, 39, 1775–1784.
35. Montoya, A.; Sendt, K.; Haynes, B. S. J Phys Chem A 2005, 109, 1057–1062.
36. Sendt, K.; Haynes, B. S. J. Phys. Chem. A 2005, 109, 8180–8186.
37. Sendt, K.; Haynes, B. S. Proc Combust Inst 2007, 31, 257–265.
38. Zhou, C.; Sendt, K.; Haynes, B. S. J Phys Chem A 2009, 113, 2975–2981.
39. Zhou, C.; Sendt, K.; Haynes, B. S. J Phys Chem A 2009, 113, 8299–8306.

40. Bongartz, D.; Ghoniem, A. F. Combust Flame 2015, 162, 544–553.
41. Rasmussen, C. L.; Hansen, J.; Marshall, P.; Glarborg, P. Int J Chem Kinet 2008, 40, 454–480.
42. Hashemi, H.; Christensen, J. M.; Gersen, S.; Glarborg, P. Proc Combust Inst 2013, 35, 553–560.
43. Glarborg, P.; Kubel, D.; Dam-Johansen, K.; Chiang, H.-M.; Bozzelli, J. W. Int J Chem Kinet 1996, 28, 773–790.
44. Alzueta, M. U.; Bilbao, R.; Glarborg, P. Combust Flame 2001, 127, 2234–2251.
45. Dagaut, P.; Lecomte, F.; Mieritz, J.; Glarborg, P. Int J Chem Kinet 2003, 35, 564–575.
46. Rasmussen, C. L.; Glarborg, P.; Marshall, P. Proc Combust Inst 2007, 31, 339–347.
47. Hindiyarti, L.; Glarborg, P.; Marshall, P. J Phys Chem A 2007, 111, 3984–3991.
48. Goos, E.; Burcat, A.; Ruscic, B.; Goos, E.; Burcat, A.; Ruscic, B. Extended Third Millennium Ideal Gas and Condensed Phase Thermochemical Database for Combustion with updates from Active Thermochemical Tables, received from Elke Goos, September, 2015.
49. Shiell, R. C.; Hu, X. K.; Hu, Q. J.; Hepburn, J. W. J Phys Chem A 2000, 104, 4339–4342.
50. Goumri, A.; Rocha, J.-D. R.; Laakso, D.; Smith, C. E.; Marshall, P. J Phys Chem A 1999, 103, 11328–11335.
51. Denis, P. A. J Sulfur Chem 2008, 29, 327–352.
52. Nagy, B.; Szakacs, P.; Csontos, J.; Rolik, Z.; Tasi, G.; Kallay, M. J Phys Chem A 2011, 115, 7823–7833.
53. Denis, P. A. Mol Phys 2010, 108, 1739–1747.
54. Peng, J. P.; Hu, X. H.; Marshall, P. J Phys Chem A 1999, 103, 5307–5311.
55. Goumri, A.; Laakso, D.; Rocha, J. D. R.; Smith, C. E.; Marshall, P. J Chem Phys 1995, 102, 161–169.
56. Ellingson, B. A.; Truhlar, D. G. J Am Chem Soc 2007, 129, 12765–12771.
57. Mousavipour, S. H.; Mortazavi, M.; Hematti, O. J Phys Chem A 2013, 117, 6744–6756.
58. Gao, Y.; Zhou, C.; Sendt, K.; Haynes, B. S.; Marshall, P. Proc Combust Inst 2011, 33, 459–465.
59. Atkinson, R.; Baulch, D. L.; Cox, R. A.; Crowley, J. N.; Hampson, R. F.; Hynes, R. G.; Jenkin, M. E.; Rossi, M. J.; Troe, J. Atmos Chem Phys 2004, 4, 1461–1738.
60. Ballester, M. Y.; Varandas, A. J. C. Int J Chem Kinet 2008, 40, 533–540.
61. Lu, C.-W.; Wu, Y.-J.; Lee, Y.-P.; Zhu, R. S.; Lin, M. C. J Chem Phys 2004, 121, 8271–8278.
62. Tsuchiya, K.; Kamiya, K.; Matsui, H. Int J Chem Kinet 1997, 29, 57–66.
63. Lee, Y.-Y.; Lee, Y.-P.; Wang, N. S. J Chem Phys 1994, 100, 387.
64. Westenberg, A. A.; DeHaas, N. J Chem Phys 1973, 59, 6685.
65. Perry, R. A.; Atkinson, R.; Pitts, J. N. J. J Chem Phys 1976, 64, 3237.
66. Michael, J. V.; Nava, D. F.; Brobst, W. D.; Borkowski, R. P.; Stief, L. J. J Phys Chem 1982, 86, 81.
67. Lafage, C.; Pauwels, J.-F.; Carlier, M.; Devolder, P. J Chem Soc, Faraday Trans 2 1987, 83, 731.
68. Tyndall, G. S.; Ravishankara, A. R. Int J Chem Kinet 1991, 23, 483.
69. Singleton, D. L.; Cvetanovic, R. J. J Phys Chem Ref Data 1988, 17, 1377.
70. Tsuchiya, K.; Yokoyama, K.; Matsui, H.; Oya, M.; Dupre, G. J Phys Chem 1994, 98, 8419–8423.
71. Mellouki, A.; Ravishankara, A. R. Int J Chem Kinet 1994, 26, 355–365.
72. Starik, A. M.; Savelieva, V. A.; Sharipov, A. S.; Titova, N. S. Combust Flame 2016, 170, 124–134.
73. Stachnik, R. A.; Molina, M. J. J Phys Chem 1987, 91, 4603.
74. Resende, S. M.; Ornellas, F. R. Phys Chem Chem Phys 2003, 5, 4617–4621.
75. Garrido, J. D.; Ballester, M. Y.; Orozco-Gonzalez, Y.; Canuto, S. J Phys Chem A 2011, 115, 1453–1461.
76. Freitas, G. N.; Garrido, J. D.; Ballester, M. Y.; Nascimento, M. A. C. J Phys Chem A 2012, 116, 7677–7685.
77. Grant, D. J.; Dixon, D. A.; Francisco, J. S.; Feller, D.; Peterson, K. A. J Phys Chem A 2009, 113, 11343–11353.
78. Turnipseed, A. A.; Barone, S. B.; Ravishankara, A. R. J Phys Chem 1992, 96, 7502–7505.
79. Ballester, M. Y.; Varandas, A. J. C. Phys Chem Chem Phys 2005, 7, 2305–2323.
80. Friedl, R. R.; Brune, W. H.; Anderson, J. G. J Phys Chem 1985, 89, 5505–5510.
81. Lovejoy, E. R.; Wang, N. S.; Howard, C. J. J Phys Chem 1987, 91, 5749–5755.
82. Wang, N. S.; Howard, C. J. J Phys Chem 1990, 94, 8787–8794.
83. Glarborg, P.; Marshall, P. Int J Chem Kinet 2013, 45, 429–439.
84. Glarborg, P.; Halaburt, B.; Marshall, P.; Guillory, A.; Troe, J.; Thellefsen, M.; Christensen, K. J Phys Chem A 2014, 118, 6798–6809.
85. Gregor, I. K.; Martin, R. L. Aust J Chem 1961, 14, 462–468.
86. Cadle, R. D.; Ledford, M. Int J Air Water Pollut 1966, 10, 25–30.
87. Hales, J. M.; Wilkes, J. O.; York, J. L. Atmos Environ 1969, 3, 657–667.
88. Becker, K. H.; Inocencio, M. A.; Schurath, U. Proc Symp Chem Kinet Data Upper Lower Atmos 1975, 205–220.
89. Glavas, S.; Toby, S. J Phys Chem 1975, 79, 779–782.
90. Glavas, S.; Toby, S. Am Chem Soc Symp Ser 1975, 17, 122–131.
91. Larin, I. K.; Spasskii, A. I.; Trofimova, E. M.; Turkin, L. E. Kinet Catal 2010, 51, 1–5.
92. Schoenle, G.; Rahman, M. M.; Schindler, R. N. Ber Bunsenges Phys Chem 1987, 91, 66–75.
93. Resende, S. M.; Ornellas, F. R. Chem Phys Lett 2001, 349, 123–130.

94. Zhou, C. Ph.D. thesis, The University of Sydney, 2009.
95. CHEMKIN PRO version 15131, Reaction Design, San Diego, CA, 2013.
96. Glarborg, P.; Bentzen, L. L. B. Energy Fuels 2008, 22, 291–296.
97. Denis, P. A. Chem Phys Lett 2004, 395, 12–20.
98. Davidson, F. E.; Clemo, A. R.; Duncan, G. L.; Browlet, R. J.; Hobson, J. H.; Grice, R. Mol Phys 1982, 46, 33–40.
99. Balucani, N.; Casavecchia, P.; Stranges, D.; Volpi, G. G. Chem Phys Lett 1993, 211, 469–472.
100. Zhou, C.; Sendt, K.; Haynes, B. S. Proc Aust Combust Symp 2007, 78–81.